Nano Energy 103 (2022) 107820

Contents lists available at ScienceDirect

Nano Energy

journal homepage: www.elsevier.com/locate/nanoen

Continuous, crystalline Sb_2S_3 ultrathin light absorber coatings in solar cells based on photonic concentric p-i-n heterojunctions

Pascal Büttner [a], Florian Scheler [a,1], Dirk Döhler [a], Maïssa K.S. Barr [a], Michael Bosch [a], Marcel Rey [b], Tadahiro Yokosawa [c], Sandra Hinz [d,e], Janina Maultzsch [d], Erdmann Spiecker [c], Nicolas Vogel [b], Ignacio Mínguez-Bacho [a], Julien Bachmann [a,*]

[a] Friedrich-Alexander University of Erlangen-Nürnberg (FAU), Chemistry of Thin Film Materials, IZNF, Cauerstr. 3, 91058 Erlangen, Germany
[b] Friedrich-Alexander University of Erlangen-Nürnberg (FAU), Institute of Particle Technology, Haberstraße 9a, 91058 Erlangen, Germany
[c] Friedrich-Alexander University of Erlangen-Nürnberg (FAU), Center for Nanoanalysis and Electron Microscopy, Institute of Micro- and Nanostructure Research, IZNF, Cauerstr. 3, 91058 Erlangen, Germany
[d] Friedrich-Alexander University of Erlangen-Nürnberg (FAU), Institute for Physics of Condensed Matter, Staudtstr. 7, 91058 Erlangen, Germany
[e] University of Hamburg, Institute for Physical Chemistry, Grindelallee 117, 20146 Hamburg, Germany

ARTICLE INFO

Keywords:
Antimony chalcogenides
Atomic layer deposition
Interface chemistry
Interfacial layers
Gradient doping
Photonic structures
Concentric semiconductor junctions

ABSTRACT

Many modern types of solar cells that rely exclusively on earth-abundant non-toxic materials include interfaces between a heavier metal chalcogenide and another type of semiconductor. Often, the chemical (adhesion) and physical (charge transfer) characteristics of those interfaces are the defining factors for the final device performance. Here, we describe that a ZnS adhesion layer is not sufficient to prevent the dewetting of Sb_2S_3 upon annealing a thin layer of it on an oxidic surface if the substrate is not planar and features highly curved surfaces. An ALD-coated sacrificial capping layer of ZnO prevents the morphological rearrangements of Sb_2S_3 during thermal crystallization and can be removed subsequently. When implemented towards a photovoltaic p-i-n heterojunction, this strategy furnishes perfect conformality of the layer stack but unsatisfactory performance. The correlation of interface chemistry with the electrical properties and the device performance identifies a reducing effect of ZnO atomic layer deposition chemistry on the Sb_2S_3 surface as the cause of Zn diffusion into the light absorbing semiconductor. This deleterious doping can be prevented by a preliminary oxidative treatment of the Sb_2S_3 surface with ozone. When applied to a structured substrate consisting of ordered arrays of nanospheres, this approach yields the first ever concentric p-i-n heterojunction solar cells with photonic light trapping effect—a geometry which in comparison with standard scattering layers'on top' inherently generates a very large refractive index contrast. In the red part of the visible spectrum, light absorption amounts to the value expected with four passes through a planar layer of the thickness used here (35 nm Sb_2S_3). This effect allows us to demonstrate >5% overall solar energy conversion efficiency with only 35 nm of a simple light absorber phase that uses no toxic, rare materials.

1. Introduction

Interface and heterojunction engineering plays a crucial role in the fabrication of electronic devices. Thoroughly designed heterojunctions allow for controlling the exchange of energy and charges across interfaces. The relevant properties here include the morphology, chemical composition and crystal structure of the semiconductors involved, which can be exploited to optimize band alignment and mitigate charge recombination at the interface. Managing these aspects allows optimizing the performance of certain materials systems in a broad range of applications such as solar energy conversion, light-emitting diodes, field-effect transistors, sensors, or batteries.

Especially in solar cells, these considerations lie at the heart of the search for 'emerging' photovoltaics, that is, alternatives to the established, traditional crystalline silicon technology. In particular, thin film photovoltaics based on CdTe and CIGS ($Cu(In,Ga)Se_2$) cells have been commercially available for years. However, the scarcity of some constituting elements (In,Ga,Te) and toxicity concerns (Cd) call for replacements [1]. One prominent proposition in that respect is the

* Corresponding author.
E-mail address: julien.bachmann@fau.de (J. Bachmann).
[1] Current affiliation: Helmholtz-Zentrum Berlin für Materialien und Energie GmbH, Young Investigator Group Perovskite Tandem Solar Cells, 12489 Berlin, Germany.

https://doi.org/10.1016/j.nanoen.2022.107820
Received 9 May 2022; Received in revised form 30 August 2022; Accepted 18 September 2022
Available online 22 September 2022

family of chalcogenide absorbers that include CZTS ($Cu_2ZnSn(S,Se)_4$), $Sb_2(S,Se)_3$ and other chalcogenide light absorbers [2–4]. Solar cells made from these materials have not achieved efficiencies comparable with the established thin film technologies so far. In cells based on those materials, overall solar energy conversion efficiencies are limited in the first place by limited open-circuit potentials (V_{oc}), which have always been significantly below the theoretically achievable value based on the radiative recombination limit. [5–9] V_{oc} losses can be caused by trapping of carriers in the bulk of the light absorbing layer or at its interfaces [10]. Minimizing the former always implies generating the highest possible crystalline quality,[6,11–13] and can additionally be achieved by thinning down the active layer [14–16]. In that case, however, maintaining sufficient light absorption (and thereby photocurrent density) must rely on generating a nanostructured ('interdigitated') heterojunction [17–21].

Interface-related losses are related to (a) deviations of the material identity (composition, phase, stoichiometry) from the bulk, [22,23] (b) frustrated bonding situations associated with the absence of adequate bonding partners across the interface, even if both materials are structurally and chemically perfect,[8,24] and/or (c) pinholes which disturb the homogeneous diode situation [25,26]. Avoiding interface-related losses, especially (c), becomes particularly challenging in the case of nanostructured heterojunctions mentioned just before, where layer conformality can only be achieved by specific deposition methods.

Atomic layer deposition (ALD) is often considered as the ideal method for achieving conformality, even on complex surfaces. Relying solely on the advantages of ALD, however, may be futile as the subsequent annealing usually required for achieving high crystalline quality can cause vast rearrangements in the film morphology. This phenomenon has been observed in striking manner in the case of Sb_2S_3, which in the absence of an adhesion layer dewets dramatically and loses continuity altogether [27]. In planar systems, a thin layer of ZnS suffices to keep Sb_2S_3 in place during annealing, [28] but highly curved (nanostructured) interfaces undermine the adhesion mediation effect of ZnS [21]. The following results delineate our strategy towards maintaining the conformality of Sb_2S_3 ultrathin coatings on substrates of arbitrarily complex shapes while allowing for the formation of very large (>10 μm) Sb_2S_3 crystals (stibnite). A thin ZnO capping layer grown by ALD at low temperature preserves the conformality of the ALD-grown amorphous Sb_2S_3 during annealing. Subsequently, ZnO is removed selectively by dilute acetic acid. The mutual thermal reactivity of Sb_2S_3 and ZnO renders it crucial to fine-tune the redox budget of the interface in order to avoid losses via mechanism (a) mentioned above at the Sb_2S_3 interface to the hole transport material in the final device. We demonstrate the success of the optimized procedure to fabricate highly efficient Sb_2S_3 solar cells in both planar and nanostructured configurations. The latter configuration is based on hexagonal arrays of interspaced silica nanospheres, which function as a photonic light trapping structures. These represent the first successful demonstration of a solar cell employing concentric p-i-n heterojunctions with a photonic light-trapping effect. This light trapping results in improved light collection in the red spectral range and enhances photocurrent density over planar solar cells, reaching high efficiencies of 5.4%.

2. Results and discussion

2.1. Preparation and structural characterization

Atomic layer deposition (ALD) is perfectly suited to the deposition of amorphous Sb_2S_3 coatings in high chemical purity and close to perfect conformality on a broad range of substrates with various chemical identities and morphological features. However, the subsequent thermal crystallization of Sb_2S_3 is highly dependent on the morphology and nature of the substrate. In extreme cases, such as alkyl-terminated surfaces, a complete dewetting of the Sb_2S_3 film to spherical stibnite particles occurs upon annealing (SI Fig. S1). In our previous work, we demonstrated how a thin interlayer of ZnS (1 nm) is able to alleviate chemical incompatibilities between oxide and sulfide and therefore prevent dewetting of Sb_2S_3 films on planar substrates (SI Fig. S1a,b), resulting in the formation of large stibnite grains the lateral size of which vastly exceeds their thickness [27,28]. Nevertheless, the mobility of Sb_2S_3 on the substrate surface remains and becomes problematic for rough or structured substrates, especially for relatively low Sb_2S_3 film thicknesses (here 35 nm). Upon annealing, the Sb_2S_3 layer retracts from convex and into concave regions on the surface, leaving the ZnS interfacial layer exposed [21]. A selection of examples is presented in the first row of Fig. 1, Fig. 1b,e,h,k.

We introduce a novel pathway to preventing excessive rearrangements of the Sb_2S_3 film during crystallization: the confinement of the amorphous Sb_2S_3 layer during the annealing process by a suitable sacrificial capping layer. In this work, ZnO is the material of choice, since it can be grown by ALD at low temperatures, has sufficient mechanical stability, and is very easy to etch with dilute acetic acid, which does not damage the stibnite layer underneath. The novel fabrication pathway based on a ZnO cap is shown schematically in Fig. 1a. On planar Si/SiO_2 substrates, the ZnO capping overlayer strategy achieves results very similar to those obtained with the ZnS interfacial underlayer only (SI Fig. S2b,c). Both options lead to similar morphologies of continuous, pinhole-free layers composed of large stibnite grains that are sufficiently large that they can be observed and characterized in an optical microscope (SI Fig. S3-6). However, the ZnS interfacial layer is no longer sufficient to maintain film conformality even in the case of slightly rougher substrates such as the transparent conductive oxide (TCO) fluorine doped tin oxide (FTO). Indeed, the tips of the $FTO/TiO_2/ZnS$ substrate become exposed after annealing (Fig. 1b), leading to potentially detrimental contacts between electron transport material (ETM) and hole transport material (HTM) in completed devices. The use of ZnO as a capping layer during annealing, on the other hand, results in conformal Sb_2S_3/ZnO layers covering the $FTO/TiO_2/ZnS$ tips (Fig. 1c), whereas the smooth surface of the crystalline Sb_2S_3 absorber layer becomes exposed as desired after etching in dilute acetic acid (Fig. 1d). Naturally, the advantages of the ZnO cap strategy become even more evident on structured substrates with larger aspect ratio, such as textured silicon (of relevance for the fabrication of tandem cells, Fig. 1e–g & SI Fig. S7), anodic aluminum oxide and TiO_2 nanotubes (relevant in the dye-sensitized and extremely thin absorber (ETA) solar cell field, Fig. 1h–j, SI Fig. S8,9), and ordered arrays of nanospheres which are interesting as photonic light trapping structures (Fig. 1k–m). The confinement by the ALD-grown ZnO layer excels on all investigated oxide nanostructures, demonstrating the versatility of our method for a vast field of applications.

2.2. Interface design and device performance optimization

To investigate the influence of the ZnO cap and the interfacial chemistry on device performance, the following samples are compared:

- the '*Ref*' devices: reference samples on $FTO/TiO_2/ZnS$ substrates with "dewetted" Sb_2S_3;
- the '*Air*' devices: samples featuring conformal Sb_2S_3 layers obtained with the sacrificial ZnO strategy (whereas ZnO is deposited after exposing Sb_2S_3 to air);
- the '$x\,min\,O_3$' ($x = 1, 3$): samples featuring conformal Sb_2S_3 layers obtained with the sacrificial ZnO strategy, whereas ZnO is deposited after exposing Sb_2S_3 to x minutes of UV/ozone treatment.

Given the significant number of devices the performance of which will be compared in the course of this manuscript, we present a full list of solar cell types with label nomenclature and full performance parameters in tabular format in the supporting information (SI Tables S1-3). In all cases, the solar cells are then completed by spin-coating P3HT and PEDOT:PSS as the hole transport material (HTM) and subsequent

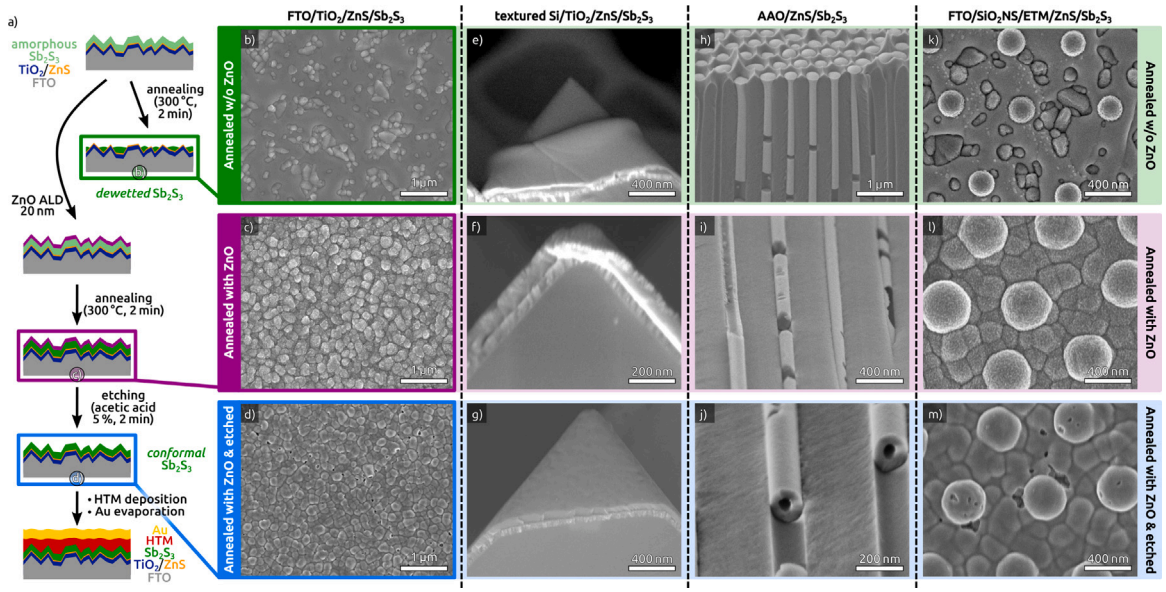

Fig. 1. Fabrication scheme (a) and the corresponding SEM images (b,c,d) for crystalline Sb_2S_3 ultrathin coatings derived from either direct annealing (b) or annealing with ZnO capping (c) and subsequent etching (d) of the as-grown amorphous Sb_2S_3 ultrathin film on standard FTO/TiO_2 substrates as commonly used in thin film photovoltaics (b,c,d) and on more complex structures, namely textured silicon (e,f,g), anodic alumina nanopores (h,i,j) and interspaced silica nanospheres on FTO substrates (k,l,m).

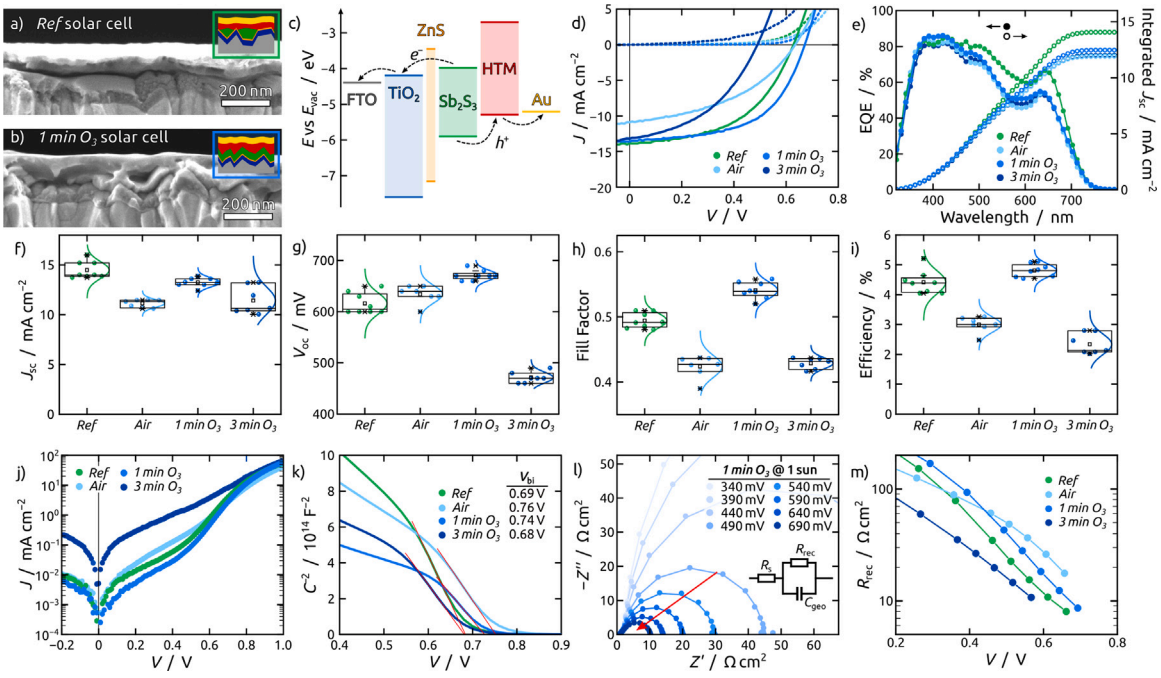

Fig. 2. (a,b) SEM cross-sections and schematic structure of solar cell devices made without (a) and with (b) employing a ZnO capping layer during annealing. (c) Schematic band diagram of the solar cell layer structure. (d) Representative *JV*-curves under 1 sun illumination (solid lines) and in dark (dashed lines). The color code for this and following panels is: green, *Ref* cells; light blue, *Air*; azure blue, *1 min O_3*; navy blue, *3 min O_3*. (e) Representative EQE spectra (filled circles) with integrated J_{sc} (empty circles). (f,g,h,i) Statistics on J_{sc} (f), fill factor (g), V_{oc} (h) and efficiency (i). (j) Dark *JV*-curves for representative devices in a semi-log plot. (k) Mott-Schottky plot of the capacitance–voltage data recorded in the dark at a frequency of 10 kHz. The built-in potentials (V_{bi}) of the respective solar cells are estimated by extrapolating the linear portion of the curve towards zero. (l) Representative Nyquist plot of impedance spectroscopy data recorded for a *1 min O_3* solar cell under 1 sun at various potentials approaching V_{oc} fitted to a Randles circuit as drawn. The red arrow indicates the evolution with increasing voltage. (m) Recombination resistance R_{rec} obtained from fitting the impedance measurements under 1 sun versus voltage.

thermal evaporation of gold contacts (Fig. 2a,b). A schematic band diagram can be seen in Fig. 2c. Unexpectedly, the *Air* devices based on conformal Sb_2S_3 layers actually show a decreased performance compared to the dewetted *Ref* solar cells (Fig. 2d). While the open-circuit potential (V_{oc}) increases slightly, the severe loss in short-circuit current (J_{sc}) and fill factor (*FF*) leads to a significant drop in efficiency (Fig. 2f–i).

Based on corresponding solar cells, the ZnO ALD and etching process alone can be excluded as the main cause for the performance losses, leaving the annealing process as the most probable origin (SI Fig. S10). In fact, varying the annealing temperature and duration shows a very clear trend for Sb_2S_3/ZnO devices (SI Fig. S11), with higher temperatures for longer durations leading to inferior device performance, while the performance of *Ref* cells is far less affected

(SI Fig. S12). This clearly points to a detrimental interface reaction and/or diffusion at the Sb_2S_3/ZnO interface.

Since the use of Sb_2O_3 as a passivating interfacial layer has been demonstrated previously, [29,30] we test the deliberate surface oxidation Sb_2S_3 by UV/ozone to avoid its direct contact with ZnO during the annealing procedure. The experimental performance results are presented in Fig. 2d–i. While 3 min of UV/ozone treatment proves to be too long, only 1 min exhibits a significant improvement over both the *Air* and the *Ref* cells. Both the *FF* and V_{oc} increase, which results in efficiencies beyond 5% for *1 min O_3* cells.

More in-depth characterization of the electrical properties of the four solar cell types reveals a significant reduction in leakage current in the dark *JV* curves (Fig. 2j) for the *1 min O_3* sample over the *Ref* cells. The improvement in the shunt resistance (R_{Sh}) is also apparent in Fig. 2d, where interestingly the *1 min O_3* sample also improves the series resistance (R_S) simultaneously: its R_{Sh} is roughly doubled with respect to *Air* whereas its R_S is almost halved (SI Fig. S13).

Mott-Schottky (MS) analysis of the capacitance–voltage data collected in the dark at a frequency of 10 kHz in a potential range from −0.3 V to +1.2 V are presented in Fig. 2k in the classical presentation $C^{-2}(V)$, to be interpreted along:

$$C^{-2} = \frac{2}{qA^2\epsilon N_D}(V_{bi} - V) \quad (1)$$

with q, A, ϵ and N_D being the elemental charge, the active device area, the permittivity, and the carrier density, respectively [31]. The choice of extracting capacitance values at a single frequency (as opposed to a fit to a full frequency-range data set) is not only standard for this type of cells, but it is also validated by the impedance spectroscopy results presented later. The built-in potentials (V_{bi}) determined from the linear section of the curves are maximized for the *Air* and *1 min O_3* samples. Increasing the duration of the UV/ozone treatment beyond 1 min results in a significant drop of V_{bi} — the maximum theoretically achievable V_{oc} value is reduced from 0.76 V to 0.68 V. Impedance spectroscopy provides complementary information collected under operation conditions (1 sun, Fig. 2l as an exemplary set of Nyquist plots for a representative *1 min O_3* at various potentials from V_{oc} towards −0.1 V). All data for the samples presented here (SI Fig. S14-17) was analyzed by equivalent circuit fitting using the simplified Randles circuit model, with its validity already demonstrated in a previous work for this exact layer stack [28]. Since both, the extracted series resistance (R_s), which is essentially dependent on the employed contact materials, as well as the geometric capacitance, depending on the device geometry and dielectric constant of the absorber material, do not substantially vary, it is the extracted recombination resistance being the parameter of interest. It is given by [32]:

$$R_{rec} = \frac{k_B T}{\beta q j_{rec}} = \frac{k_B T}{\beta q j_0} exp(-\beta \frac{qV_F}{k_B T}) \quad (2)$$

with k_B, T, β, q, j_{rec}, j_0, V_F being the Boltzmann-constant, temperature, ideality factor, elementary charge, recombination current, dark saturation current and the applied voltage, taking into account the voltage drop by the series resistance, respectively.

Hence, R_{rec} allows to make assumptions on the recombination rate as well as on the ideality of this process. Fig. 2m shows R_{rec} against the applied DC voltage for the different surface treatments. In short, the improved performance of *1 min O_3* devices is mirrored by an increase of the recombination resistance, while maintaining ideal diode behavior in comparison to the *Ref* devices. In opposite, excess ozone treatment (*3 min O_3*), as well as *Air* result in a decrease of the recombination resistance at low voltages; additionally, the curves show less ideal diode behavior close to open circuit, manifested by a more linear slope which is pointing towards extraction limitations.

2.3. Chemical and physical investigation of the Sb_2S_3

The chemical effects of UV/ozone treatment and annealing are revealed by X-ray photoelectron spectroscopy (XPS) investigations performed at distinct stages of fabrication. The surface of as-grown amorphous Sb_2S_3 consists of mostly pure Sb_2S_3 (SI Fig. S18) with only minor contributions of Sb-O (after exposure to air) with the majority of the observed O 1s peak being attributed to adventitious carbon species (Fig. 3a). The contribution of Sb_2O_3 increases dramatically with increasing duration of the UV/ozone treatment. Simultaneously, the formerly pure S^{2-} doublet of the S 2p region splits, showing the formation of S-S bonds (Fig. 3b). Whether this signal originates from elemental sulfur, S^0 (as labeled in Fig. 4b for simplicity) or from some polysulfides, S_n^{2-}, $n \leq 2$, cannot be determined unambiguously, but is not of prime importance for our study. The relevant message is that the sulfide component of Sb_2S_3 becomes oxidized with Sb_2O_3 formed as the by-product, as opposed to a simple anion exchange (hydrolysis) reaction which would result in the loss of sulfide (unoxidized S^{2-} as H_2S). If the treatment is allowed to proceed for too long, the oxidation of sulfur (S^0) eventually proceeds to sulfate (SO_4^{2-}). Fig. 3c summarizes how the relative contributions of the different species observed in the Sb 3d and S 2p peaks evolve as a function of the UV/ozone treatment duration.

Let us now explore how this oxidative surface chemistry of Sb_2S_3 in the preliminary step evolves after the ZnO capping and removal procedure as in the finished solar cells. In the case of the *Ref* sample, the Sb_2S_3 surface is chemically identical to its state immediately after ALD (SI Fig. S19 and Fig. 3d, to be compared with Fig. 3a). Unexpectedly, overgrowing the amorphous Sb_2S_3 layers with ZnO (either directly without breaking vacuum, *Vac*, or after opening the chamber to air, *Air*) then annealing and etching leads to the formation of large quantities of antimony in a lower oxidation state, Sb^0, on the Sb_2S_3 surface. In parallel to this, the presence of zinc on the surface is obvious in significant amounts in both *Vac* and *Air* samples in Fig. 3e. We note that this Zn cannot be associated with remnants of ZnO, since the O 1s signal is vanishingly small. In other words, Zn must have been incorporated into the upper layers of the Sb_2S_3 phase in some form. Perhaps even more startling is the complete absence of any trace of Zn in Sb_2S_3 films that were subjected to UV/ozone treatment before ZnO ALD (Fig. 3e). Simultaneously, the spectra also show far reduced contributions of Sb^0 as compared to *Vac* and *Air* samples (Fig. 3d). In fact, for longer UV/ozone durations of more than 3 min, residual Sb-O bonding can be observed instead of Sb^0. The absence of Sb-O for 1 min of UV/ozone treatment is remarkable, since the UV/ozone treated amorphous film showed ~60% of oxide contribution. At this step, all samples feature sulfur as S^{2-} exclusively, and all traces of other oxidation states previously observed, be they in the form of S^0 or SO_4^{2-} have disappeared (SI Fig. S19b). This first set of XPS observations establishes a correlation between:

- the formation of oxidized S upon ozone treatment,
- the absence of reduced Sb after ZnO capping and removal procedure, and
- the absence of Zn after that same procedure.

Let us now investigate how reduced Sb and incorporated Zn relate to one another, and how they affect the physical properties of the semiconductor stack. The distinct behavior of Sb and Zn XPS signals upon sputtering the samples with argon ions (Fig. 3f, SI Fig. S20) reveals starkly contrasting chemical fates for Sb and Zn. All non-sulfide contributions to the Sb 3d signal disappear (apart from the small Sb^0 amount always generated by sputter damage), suggesting that antimony oxide and reduced antimony are exclusively present at the very surface. However, the Zn signal remains after sputtering, with slightly decreased intensity, which means that is has diffused into the Sb_2S_3 layer. This diffusion is thermally driven, as proven by a set of control

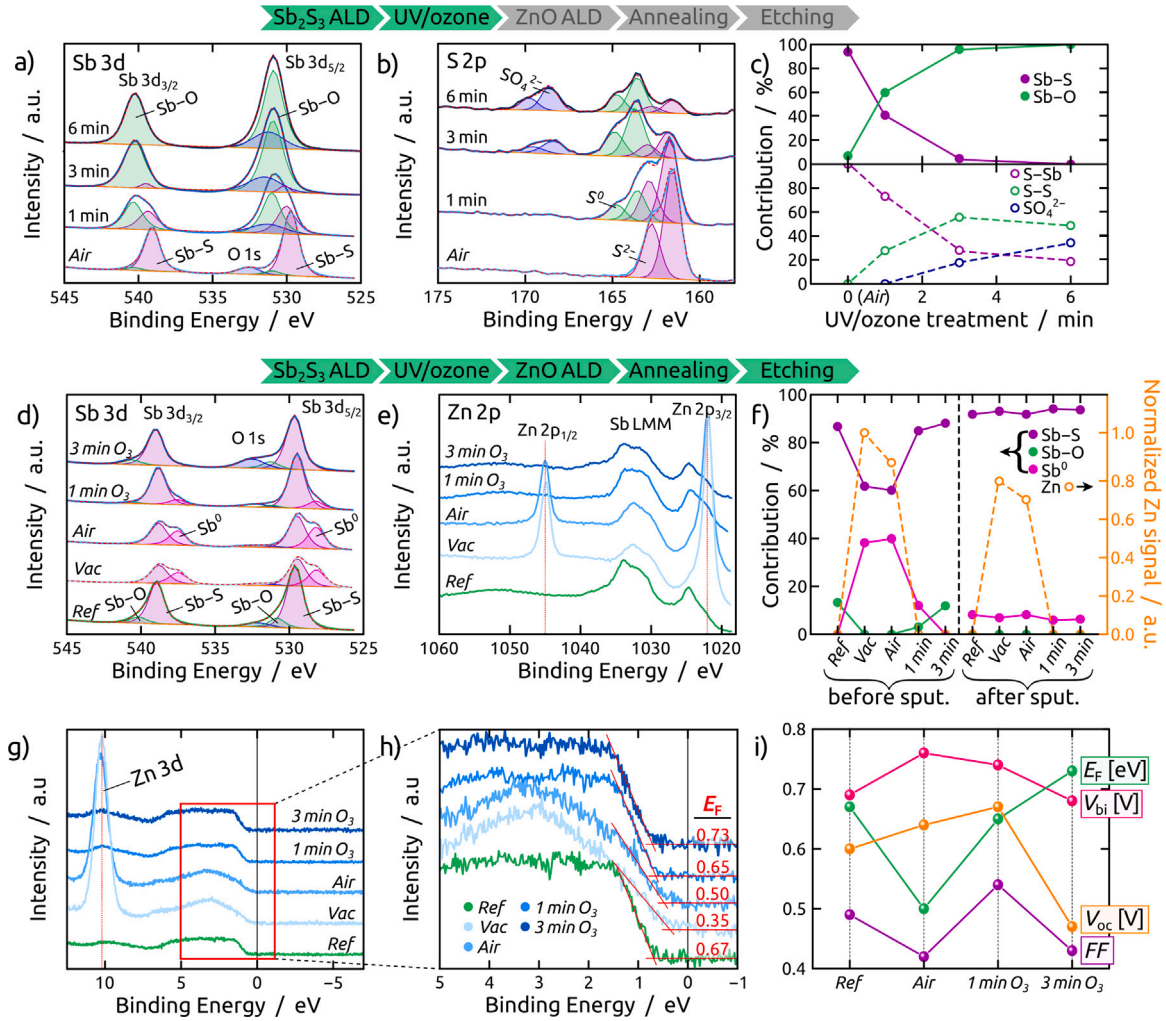

Fig. 3. X-ray photoelectron spectroscopy (XPS) results on the surface of Sb_2S_3 films at two distinct points of the fabrication procedure. (a) Sb 3d and O 1s and (b) S 2p regions of amorphous Sb_2S_3 films after various durations of the UV/ozone treatment. (c) Relative peak areas of the different species observed in the Sb $3d_{5/2}$ and S $2p_{3/2}$ peaks versus UV/ozone treatment duration. (d) Sb 3d and O 1s and (e) Zn 2p regions of native annealed Sb_2S_3 films as well as Sb_2S_3 films that were subjected to different durations of UV/ozone treatment before capping with ZnO, annealing and etching. (f) Relative peak areas of the different species observed in the Sb $3d_{5/2}$ peak and normalized intensity of the Zn $2p_{1/2}$ peak for the investigated films before and after removal of the uppermost surface layer by argon ion sputtering. (g) Valence-band XPS (VBXPS) spectra and (h) close-up of the region indicated in (g) with the respective positions of the Fermi level (E_F) above the valence band maximum (VBM). (i) Summary of key parameters influencing solar cell performance obtained from *JV*-curves (V_{oc}, *FF*), MS analysis (V_{bi}) and VBXPS (E_F).

experiments in which *Air*-type samples annealed to increasing temperatures exhibit increasing XPS Zn 2p signal intensity (SI Fig. S21,22). These annealing temperatures and Zn contamination degrees exhibit an inverse correlation to device performance, SI Fig. S11. No such correlation is found in the absence of ZnO cap, SI Fig. S12. Also, acetic acid treatment of Sb_2S_3 has no influence on either device performance or surface chemistry, SI Fig. S13,23.

The influence of what amounts to Zn gradient doping on the band structure is apparent in the valence band XPS (VBXPS) spectra of *Ref* samples and ZnO-capped samples with different interface treatments (Fig. 3g,h). Unaltered, *Ref* Sb_2S_3 films (or their XPS-accessible near-surface region, to be specific) appears to be slightly p-type in nature with the Fermi level (E_F) positioned 0.67 eV above the valence band maximum (VBM). *Vac* and *Air* samples, which both feature significant Zn diffusion during annealing, exhibit a shift of E_F towards the VBM, or in other words, enhanced p-type doping. This observation is more pronounced for the *Vac* sample, which proves that Sb^0 is not the direct cause of doping (but Zn instead), given that the Sb^0 signal is similar in both *Vac* and *Air*. Treating the Sb_2S_3 films with 1 min of UV/ozone before ZnO ALD, annealing and etching results in a E_F position close to its original value in native *Ref* Sb_2S_3. Longer durations of the UV/ozone treatment result in a further shift of E_F towards the middle of the Sb_2S_3 band gap, probably introduced by the presence of residual oxide on the Sb_2S_3 surface.

Taken together, the results obtained from device performance, MS and VBXPS provide a complete picture, summarized in Fig. 3i. Although the Zn gradient doping of Sb_2S_3 renders the surface of *Air* samples more p-type and therefore results in a larger V_{bi}, efficient hole extraction is hindered by an energetic barrier, resulting in a drop in *FF*. Excessive oxidative treatment of the Sb_2S_3 surface results in the presence of residual Sb_2O_3 after the whole ZnO capping procedure, which acts as a recombination center and reduces V_{oc} (and *FF*) much below V_{bi}.

2.4. Crystallinity and purity of Sb_2S_3

High resolution transmission electron microscopy (HRTEM, Fig. 4) cross-sections of Sb_2S_3 films after annealing under the ZnO capping layer and subsequent wet etching complement the information extracted from XPS. Here, the stibnite films are covered by a thin gold layer to avoid electrostatic charging. In the optimized *1 min O_3* sample, the Sb_2S_3 films is composed of large crystals that span the entire film thickness and remain perfect up to the very surface (Fig. 4g,h). Energy-dispersive X-ray spectroscopy (EDX) mappings and depth profiles show

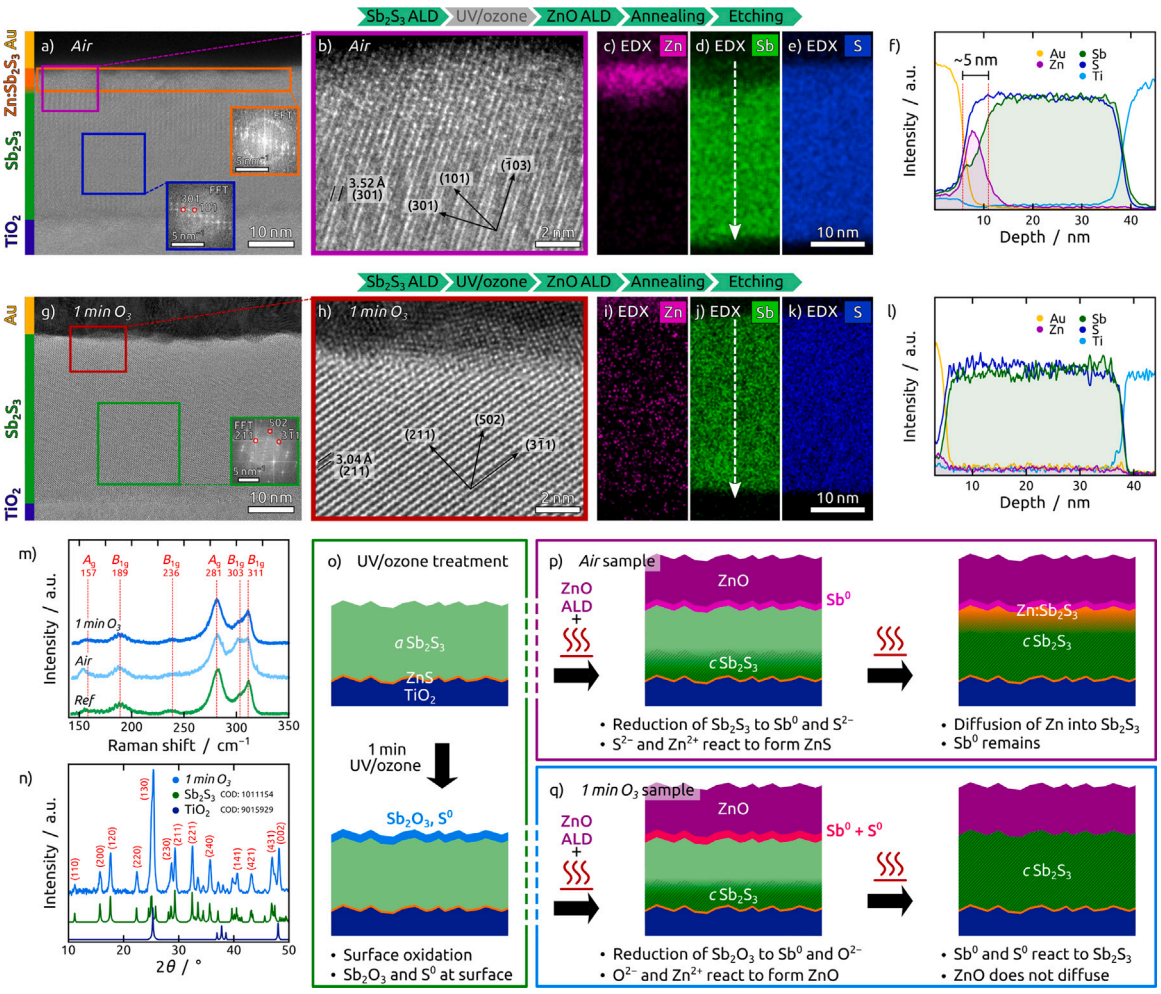

Fig. 4. (a–f) Transmission electron microscopy (TEM) analysis of Sb_2S_3 film cross sections for *Air* samples. (a) High-resolution TEM (HRTEM) image of the full film thickness with fast Fourier transforms (FFTs) of the areas indicated in the image. (b) Close-up of the upper Sb_2S_3 surface as indicated in (a). (c–e) Energy dispersive X-ray (EDX) mapping of the Sb_2S_3 film for the elements Zn (c), Sb (d) and S (e). (f) EDX line trace along the film thickness top to bottom as indicated in (d). (g–l) TEM analysis of Sb_2S_3 film cross sections for samples submitted to *1 min* O_3 treatment before ZnO ALD. (g) HRTEM image of the full film thickness with FFT of the area indicated in the image. (h) Close up of the upper Sb_2S_3 surface as indicated in (g). (i–k) EDX mapping of the Sb_2S_3 film for the elements Zn (i), Sb (f) and S (k). (l) EDX linetrace along the film thickness top to bottom as indicated in (j). (m) Raman spectra recorded for *ref*, *1 min* O_3 and *3 min* O_3 Sb_2S_3 films on quartz substrates. (n) Grazing-incidence X-ray diffraction (GIXRD) dataset for a *1 min* O_3 Sb_2S_3 film on TiO_2, with labels according to the calculated powder patterns for TiO_2 (anatase, COD:9015929) and Sb_2S_3 (stibnite, COD:1011154). (o–q) Schematic depiction of the mechanisms at play during UV/ozone treatment and annealing of amorphous Sb_2S_3 films with ZnO capping. (o) Oxidation of the Sb_2S_3 surface to form a thin layer containing Sb_2O_3 and S^0. (p) Stepwise evolution upon annealing of *Air* samples with ZnO capping layer. (q) Stepwise evolution upon annealing of *1 min* O_3 samples with ZnO capping layer.

the expected absence of Zn and a homogeneous distribution of Sb and S along the film thickness (4i–l and SI Fig. S24). In the absence of the UV/ozone treatment, however (*Air* sample), similarly large stibnite grains are present but yield to smaller crystallites in the verge of the top film surface (Fig. 4a,b and SI Fig. S25). This polycrystalline layer combines Sb and S contents with significant amounts of Zn, as observed in EDX maps (Fig. 4c–e and SI Fig. S26) and lines (Fig. 4f), and in line with XPS data. The S signal intensity is constant from top to bottom of the sulfide layer, while the Sb and Zn signals complement each other. The mixed layer consists of unequal grains as opposed to a perfectly smooth film but has an average thickness of approximately 5 nm (SI Fig. S27).

The Raman spectra of *Ref*, *Air*, and *1 min* O_3 films (Fig. 4m) show the Sb_2S_3 vibrational modes expected from previous reports on ALD-grown Sb_2S_3 [27]. The frequencies and intensities of the Raman modes vary slightly, but do not show any indication for Zn doping into the bulk of the scattering volume. The different relative intensities may be due to different crystallographic orientations of individual grains within the film (remember SI Fig. S3-6). X-ray diffraction data collected in grazing incidence (GI-XRD) further document the high crystalline quality of the sample and the absence of undesired phase in measurable amounts (Fig. 4n).

At this point, all information collected by XPS, HRTEM, EDX, XRD, and Raman spectroscopy allow us to draw a complete picture of the interface chemistry, Fig. 4o–q. Ozone treatment of the originally clean, amorphous as grown Sb_2S_3 yields to the formation of surface Sb_2O_3 and reduced polysulfides or elemental sulfur, S^0 (Fig. 4o). In the absence of the ozone treatment (horizontal axis, Fig. 4o–p), annealing of Sb_2S_3 covered by ALD-ZnO results in the superficial reduction of Sb_2S_3 with formation of elemental Sb^0. This reduction is concomitant with the motion of Zn^{2+} into the sulfide layer to balance charges, which can subsequently diffuse into the Sb_2S_3 under thermal activation. However, if the same annealing is performed of ZnO-covered and pre-oxidized Sb_2S_3, then the Sb^0 formation is counter-balanced by the S^0 present already. Accordingly, Zn^{2+} regenerates ZnO upon reduction of Sb_2O_3. This stable phase is not prone to Zn^{2+} diffusion during the subsequent thermal step, so that only pure ZnO and Sb_2S_3 phases remain. The last piece of information needed to complete the picture is the source of reducing equivalents from the ALD-ZnO phase. Scientists familiar with ALD chemistry will certainly be aware of the reducing power of diethylzinc used as the zinc source in ALD [33]. Although its reactivity

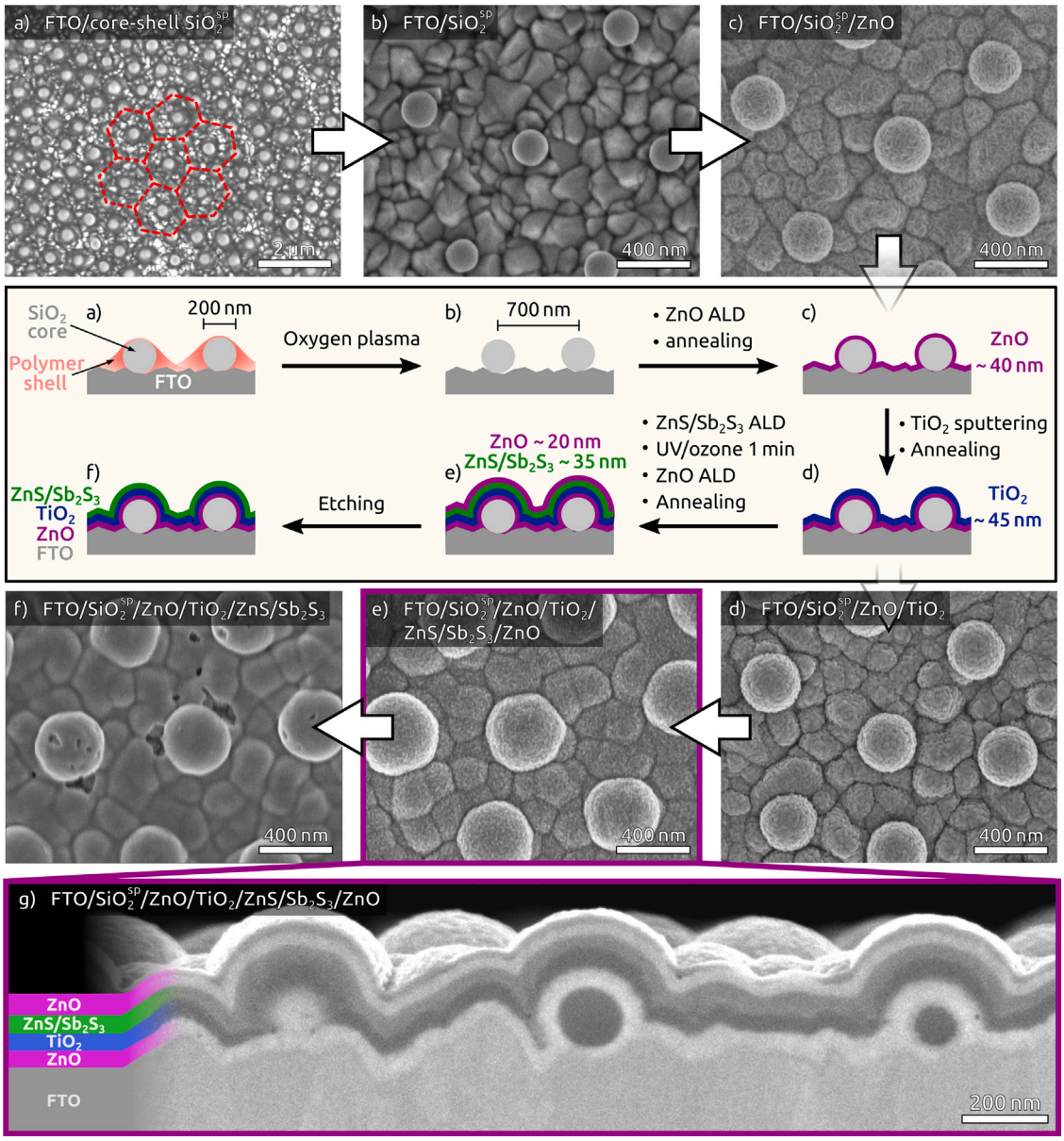

Fig. 5. Fabrication of photonic nanostructures used as electrodes for structured solar cells: schematic description (central panel), accompanied with corresponding SEM micrographs taken after each fabrication step. (a) Hexagonal monolayer of core–shell SiO_2/Polymer nanospheres on an FTO substrate. (b) Interspaced SiO_2 nanospheres on FTO after removal of the polymer shell by O_2 plasma. (c) ETM-covered photonic nanostructure after ZnO ALD and (d) TiO_2 sputtering. (e) ZnO capped absorber layer after ZnS/Sb_2S_3 ALD, UV/ozone treatment (1 min), ZnO ALD and annealing. (f) Exposed Sb_2S_3 surface after removal of the ZnO capping layer. (g) Polished SEM cross-section of fabrication step (e). The thin darker layer on top of the ZnO capping layer appears due to redeposition during cross-section polishing.

is theoretically meant to be purely of acid-base nature in combination with water to generate ZnO, XPS analysis of the ALD-ZnO phase evidences the presence of carbon in significant amounts even after sputter-cleaning (SI Fig. S28).

2.5. Application to the fabrication of concentric PV heterojunctions

We now have all tools at our disposal to fabricate perfectly conformal, highly pure Sb_2S_3-based nanostructured solar cells. We choose ordered arrays of interspaced silica nanospheres ($SiO_2{}^{sp}$) as our testbed, which will demonstrate the success of the methods described above in cases of substrate with highly curved surfaces, and their relevance towards the preparation of cells with photonic light-trapping structures [34]. A monolayer of silica-polymer core–shell spheres is first deposited onto the FTO substrate using Langmuir–Blodgett. Subsequently, the organic polymer shell is removed using oxygen plasma, leaving a well-ordered, non-close packed $SiO_2{}^{sp}$ ($d \sim 200$ nm) array with large grains of hexagonal symmetry and a pitch of ~700 nm (Fig. 5a,b and SI Fig. S29–31) [35]. For the electron transport material (ETM), we will compare the following configurations:

- the '*TiO_2*' devices will contain a sputter-coated TiO_2 ETM;
- the '*Dew.*' devices will serve as a comparison and contain the same sputter-coated TiO_2 ETM but do without ZnO capping procedure in the subsequent steps;
- the '*ZnO/TiO_2*' devices will combine an ALD-deposited ZnO layer with sputter-coated TiO_2 as the dual ETM.

The *ZnO/TiO_2* dual layer combines the advantages of efficient electron extraction by sputter-coated TiO_2 and conformal coating by ALD-deposited ZnO, which improves both electron transport to the TCO as well as hole blocking capabilities. Neither ALD-ZnO only nor ALD-TiO_2 achieve the same performance in planar devices (SI Fig. S32,33).

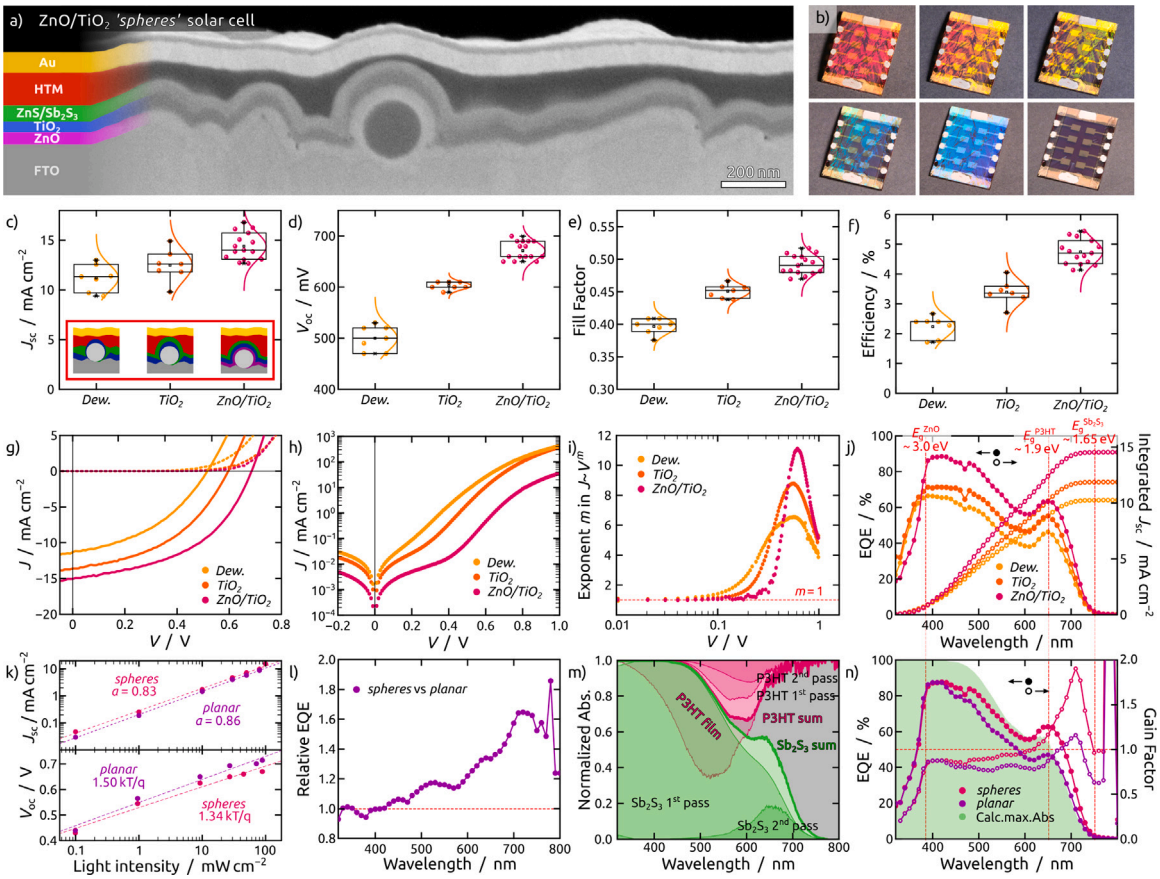

Fig. 6. (a) Polished SEM cross-section of the completed *spheres* solar cell composed of the layer stack FTO/$SiO_2{}^{sp}$/ZnO/TiO_2/ZnS/Sb_2S_3/HTM/Au. The thin darker layer on top of the gold electrode appears due to redeposition during cross-section polishing. (b) Photographs of a finished *spheres* solar cell with light incident under different angles showing the iridescence of the photonic structure. (c–f) Statistics on the performance of the different types of 'photonic' solar cells, namely J_{sc} (c), V_{oc} (d), fill factor (e) and efficiency (f). (g) Representative *JV*-curves under 1 sun illumination (solid lines) and in dark (dashed lines). (h) Semi-log plot of the dark *JV* curves shown in (g). (i) 1st derivative of the log–log plot of the dark *JV* curves revealing the power law relationship in the dark curves. (j) EQE and integrated J_{sc}. (k) log–log plot of J_{sc} versus light intensity (upper panel) and ideality factor (n_{id}) derived from the slope of V_{oc} plotted against logarithmic light intensity (lower panel). (l) Relative EQE enhancement for *spheres* cells versus *Ref* and *planar* devices. (m) Contributions of absorption in the Sb_2S_3 absorber and P3HT (parasitic) calculated for a *planar* solar cell with an absorber thickness of 35 nm without the influence of scattering. (n) EQE and corresponding optical enhancement factor (OEF) calculated by dividing the EQE by the maximal absorption calculated in (m). The calculated maximal absorption is indicated as a green shade.

The subsequent steps of preparation involve the (now familiar) ALD of ZnS, ALD of amorphous Sb_2S_3, UV/ozone treatment, ZnO ALD, annealing, and wet etching (Fig. 5c–f). Spin-coating of P3HT and PEDOT:PSS as the HTM layer completes the formation of concentric $ZnO/TiO_2/ZnS/Sb_2S_3$/P3HT n-i-p heterojunction surrounding the $SiO_2{}^{sp}$ core.

2.6. Photonic light trapping effect in structured ultrathin absorber solar cells

After the final evaporation of Au as the rear electrical contact, the devices are functional and display the close to perfect structure shown in cross-section in Fig. 6a. On a macroscopic scale (Fig. 6b), these structured cells display a strong iridescence due to the oscillation of the refractive index over the lateral dimensions ($n(Sb_2S_3) \geq 3$). Let us start by demonstrating the superior performance of the *ZnO/TiO₂* system for extracting electrons (Fig. 6c–j), before turning to the characterization of the photonic effect (Fig. 6k–n) in the following paragraph.

In the simplest preparation scheme, employing TiO_2-covered nanospheres without the sacrificial ZnO capping layer (*Dew.* in Fig. 6) yields large areas of direct ETM-HTM contact due to the uncovered SiO_2/TiO_2 spheres after dewetting upon crystallization (SI Fig. S34). Employing conformal Sb_2S_3 layers generated with the ZnO cap procedure prevents the detrimental appearance of ETM-HTM contacts, yet one disadvantage of sputtered TiO_2 becomes apparent, namely the lack of conformality. Introducing a ZnO layer by ALD underneath it provides conformal coverage of the nanospheres. Fig. 6a and SI Fig. S35 clearly show how the sputtered TiO_2 layer becomes very thin on the sides of the spheres, and the ALD-ZnO layer ensures continuity in this region. Complementing TiO_2 with ZnO in this manner is important in two respects. First, it facilitates charge transport within a continuous phase, and second, it ensures the absence of pinholes that would be deleterious to the hole blocking function (SI Fig. S36). The semi-log plots of the dark *JV*-curves (Fig. 6h) and the exponent derived as the derivative of the log–log plots (Fig. 6i and SI Fig. S37) attest to the improved electrical properties. In terms of diode quality, the sphere-based *ZnO/TiO₂* system reverts to the characteristics of the optimized planar devices presented in Fig. 2i (see also SI Fig. S38). This is reflected in the energy conversion performance parameters. The dual-ETM nanosphere-based solar cells show vast improvements with respect to their simpler counterparts *Dew.* and *TiO₂* in all three important device parameters (J_{sc}, V_{oc} and *FF*), reaching a high V_{oc} beyond 700 mV and a champion efficiency of 5.4% (Fig. 6c–f). This value achieved with a 35-nm thick Sb_2S_3 light absorber layer represents a moderate absolute performance loss with respect to the world records established with this same material, namely 7.5% in a mesoporous system [36] and 7.1% in a planar cell [8]. This moderate loss is to be placed in the perspective of the major gains in material efficiency achieved with our 35-nm layer with respect to the 1.3 μm mesoporous layer and 146 nm absorber layer thicknesses, respectively. In comparison to the planar case, our nanosphere-based system reduces material consumption by

three quarters while losing only one quarter efficiency. The external quantum efficiency (EQE) spectra evidence the improvement of charge extraction over the whole visible range with the *ZnO/TiO$_2$* procedure. The spectral shape of the EQE corresponds to the expectation for this type of ultrathin absorber solar cells, based on the bandgaps of Sb_2S_3 and P3HT (SI Fig. S39) [27].

Let us now turn to a comparison of this optimized nanosphere-based system with its planar counterparts (the *ZnO/TiO$_2$* sample will be called '*spheres*' in this context from now on). The power laws (Fig. 6k) demonstrate that planar ('*planar*') and *spheres* cells are governed by the same recombination mechanisms (see also SI Fig. S40,41). This is different from the situation observed in solar cells based on large specific surface area. In such 'interdigitated' approaches, increased light absorption by increased interfacial area is achieved at the expense of charge collection efficiency, which suffers from increased interfacial recombination [37]. The direct comparison of photon-to-electron conversion efficiency is provided by the comparison of the respective EQE spectra. Dividing the EQEs of reference *planar* (SI Fig. S42) and *sphere* cells (Fig. 6j) shows how the concentric nanostructures increase light harvesting by the photonic effect (Fig. 6l). Current generation is enhanced across the majority of the solar spectrum, with the largest improvement in the red near the bandgap (1.65 eV or 750 nm, where the absorption coefficient is smallest). We note that the photonic structure allows for achieving gains with respect to the planar situation, which is distinct from simply increasing the thickness of a planar absorber. Indeed, in the latter situation gains in the red are diminished by losses in the violet related to transport losses (as already observed in previous studies) [27]. Can the photonic light trapping gains be quantified directly? Fig. 6m derives the maximum possible absorption within the active absorber layer for an Sb_2S_3 thickness of 35 nm, calculated without taking scattering effects into account but with a potential double pass of light through the absorber (after reflection off of the Au electrical contact). Parasitic absorption by P3HT (pink curves on an inverse scale) does not affect the fruitful absorption by Sb_2S_3 in the first pass, but it significantly affects how much light is left for the second pass. It causes the EQE dip around 600 nm, which is not observed with 'classical' thin-film heterojunction cells featuring much thicker light absorber layers. When compared to this maximum possible absorption (green shade in Fig. 6n), the experimentally determined EQE of a *planar* device (purple curve) follows closely with an almost constant near-unity ratio. A minor maximum above unity near 720 nm is the result of scattering by the rough FTO substrate. The photonic structure, however, generates much more significant gains (pink curve in Fig. 6n). Between 600 and 750 nm, it allows for a constant increase in light absorption without a corresponding increase in the amount of light absorbing material used. In fact, the gain factor (with respect to the calculated double pass) almost reaches 2, which amounts to saying that at 720 nm, one given Sb_2S_3 thickness d absorbs not $\alpha(\lambda) \cdot d$ but $4 \cdot \alpha(\lambda) \cdot d$ instead.

3. Conclusions

In summary, we demonstrate a novel unique method to achieving conformal layers of highly pure Sb_2S_3 absorber layers on poorly adhesive underlying oxide substrates. The method relies on a sacrificial ZnO capping layer to confine the as-grown amorphous Sb_2S_3 layer during the annealing and crystallization process. This technique renders the crystallization behavior of Sb_2S_3 mostly independent of the substrate chemistry and morphology and allows for achieving conformal stibnite layers on virtually any nanostructure accessible by ALD. We note that light scattering layers are certainly not new in the photovoltaics field. Beyond the classic pyramids used in the silicon PV field, they mostly consist of disordered layers of particles featuring a broad size and shape distribution. Scattering layers obtained with a high degree of order by nanosphere lithography have also been applied in the emerging PV field, however they have so far always been placed on top of the full functional semiconductor stack (or underneath it). With the unique preparative method enabled now by our detailed insight into the interface chemistry, we offer the novel ability to integrate ordered arrays of spheres directly into the semiconductor stack, thereby generating a concentric p-i-n junction. The high refractive index of stibnite (tabulated value 2.65) generates an excellent contrast which would be extremely difficult to achieve with a photonic structure on top of the solar cell (a geometry which requires transparent materials to be used).

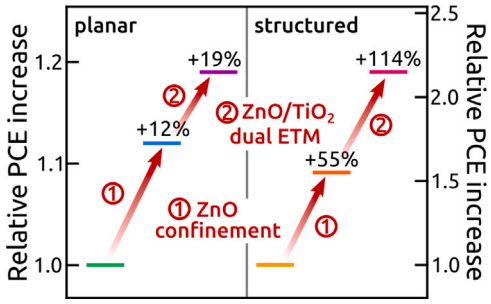

Fig. 7. Summary of the relative performance improvements achieved in this study for both planar and structured solar cells by ZnO-confined crystallization and utilization of the ZnO/TiO$_2$ dual-ETM.

As one specific application of this novel approach, we demonstrate the increase of light absorption and carrier generation without increase in material thickness or interface recombination. Fig. 7 summarizes the gains achieved by optimizing the chemical nature and geometry of the Sb_2S_3/HTM interface in a systematic manner along both the manifolds of planar and structured solar cells. These results focus on Sb_2S_3 as a wide-bandgap sulfide applicable to the top cell in tandem devices, but also as a model system for $Sb_2(S,Se)_3$ and other heavy chalcogenides. Furthermore, the insight presented here will be useful for a wealth of applications employing ultrathin sulfide phases on structured substrates, given that the results highlight a quite generally applicable strategy, namely the fine-tuning of an interface at the atomic scale. Intentionally generating controlled amounts of oxidized or reduced species at the interface allows one to generate gradient doping or block it, and to adjust Fermi levels and band alignments. The Sb_2S_3/ZnO interface can be considered as a closed-space, two-dimensional 'nanocrucible' in which thermal reactions of redox and non-redox nature can be carried out with outstanding stoichiometric and thermal control. Such approach might become of general interest for the generation of two-dimensional materials and devices.

4. Experimental

4.1. Device fabrication

Fluorine doped tin oxide (FTO) coated glass slides with 10 Ω/sq are purchased from Solaronix. The substrates are patterned by etching with zinc powder and HCl (2 M) for 10 min and subsequently cleaned by sonication in detergent (Hellmanex III, 2%), acetone, isopropanol and DI water, respectively, for 5 min each. UV/ozone cleaning (Novascan PSD-UV4) is performed for 30 min right before further use.

For samples that employ ZnO as dual or sole ETM, a compact layer of ZnO with a thickness of 40 nm is grown in a hot-wall ALD reactor (Gemstar-6 XT, Arradiance) with diethylzinc (DEZ, 95%, abcr) and millipore water as precursors and nitrogen as carrier gas. Both precursors are kept at room temperature and the reaction chamber is heated to 120 °C. The pulse times are 0.15 s for DEZ and 0.3 s for water with exposure and pumping times of 30 and 60 s, respectively.

45 nm of TiO_2 are deposited as ETM by radio frequency magnetron sputtering (CRC 622 model, Torr International, Inc.) from an TiO_2 target (99.99%). The working pressure, base pressure and power density

are 0.3 Pa, 1 × 10^{-4} Pa and 2.5 W cm^{-2}, respectively, resulting in a deposition rate of 0.1 Å/s. The working gas is argon (99.999%) at a flow rate of 5 sccm. The as-grown amorphous TiO_2 films are crystallized to anatase phase by annealing on a hotplate at 500 °C for 30 min in ambient atmosphere.

Atomic layer deposition of ZnS, Sb_2S_3 and ZnO capping layers are performed on UV/ozone cleaned substrates (30 min) in a home-made hot-wall ALD reactor. The precursors are diethylzinc (DEZ, 95%, abcr), tris(dimethylamido)antimony (TDMASb, 99.99%, Sigma Aldrich), H_2S (3% in N_2, Air Liquide) and millipore water. All precursors are kept at room temperature, except for TDMASb, which is heated to 40 °C to create sufficient vapor pressure. 9 cycles of ZnS (1 nm) are deposited by ALD at 150 °C with pulse, exposure and pumping times of 0.2 s, 30 s and 40 s for both DEZ and H_2. Thereafter the chamber is cooled to 120 °C for Sb_2S_3 deposition (600 cycles, 35 nm) without breaking vacuum. The exposure and pumping times were 15 s each, with pulse times of 1.5 s and 0.2 s for TDMASb and H_2S, respectively. Except for the cases with immediate ZnO deposition (*Vac*-sample), the ALD is cooled to room temperature before opening. Samples with UV/ozone treatment ($x\,min\,O_3$) are exposed to UV/ozone (Novascan PSD-UV4) that is operated using oxygen from ambient air for 1-6 min as stated in the main text. Deposition of the ZnO capping layer ALD is performed at 120 °C for 200 cycles (20 nm), with a pulse, exposure and pump duration of 0.2 s, 15 s and 15 s, respectively. After ZnO deposition, the ALD reactor is cooled to room temperature before opening. The as-grown amorphous Sb_2S_3 layers are converted to stibnite phase by annealing on a hotplate in an N_2-filled glovebox at 300 °C for 2 min. The ZnO capping layer is removed after annealing by etching in 5% acetic acid solution for 2 min. The samples are then rinsed with 3% acetic acid and DI water and blown dry with nitrogen.

A hole selective layer of poly-3-hexylthiophene (P3HT, regioregular, Sigma Aldrich, 15 mg/mL in chlorobenzene) is deposited by dynamic spin coating 50 μL at 6000 rpm for 1 min in ambient atmosphere and then dried on a hotplate in an N_2-filled glovebox at 90 °C for 30 min. Poly(3,4-ethylenedioxythiophene) polystyrene sulfonate (PEDOT:PSS, HTL Solar, Ossila) is spin coated at 6000 rpm for 1 min with an acceleration of 6000 rpm/s and again dried at 90 °C for 30 min in an N_2-filled glovebox. 80 nm of gold are deposited by thermal evaporation through a shadow mask with an active device area of 0.075 cm^2.

For samples that employ TiO_2 by ALD as ETM, a compact layer of amorphous TiO_2 with at thickness of 20 nm is grown in a hot-wall ALD reactor (Gemstar-6 XT, Arradiance) with titanium tetraisopropoxide (TTIP, 97%, Alfa Aesar) and millipore water as precursors and nitrogen as carrier gas. TTIP is heated to 70 °C, water is kept at room temperature and the reaction chamber is heated to 150 °C as described elsewhere [38]. The as-grown amorphous TiO_2 films are crystallized to anatase phase by annealing on a hotplate at 500 °C for 30 min in ambient atmosphere.

4.2. Core–shell nanosphere synthesis

The detailed synthesis of SiO_2-PNIPAM core–shell nanospheres is described elsewhere [35]. In brief, silica-PNIPAM core–shell nanospheres were obtained by surface functionalization of Stöber silica cores (d = 200 nm) with methacrylate moities to anchor the polymer shell to the surface. Then, a PNIPAM microgel shell (5 mol% BIS) was added onto the cores in a one-pot, batch method and overgrown by a continuous feeding of additional monomer and cross-linker.

4.3. Deposition of silica nanosphere array

A Teflon Langmuir trough (Kibron, Microtrough G2, area = 324 cm^2) equipped with two Teflon barriers system is used to prepare the monolayers of silica-PNIPAM core–shell spheres. A Wilhelmy plate is used to measure the surface pressure during the simultaneous compression and deposition process. FTO coated glass slides with dimensions 2.0 x 2.5 cm^2 are cleaned by sonication in detergent (Hellmanex III, 2%), acetone, isopropanol and DI water, respectively, for 5 min each. These substrates are exposed to oxygen plasma (Diener) for 5 min right before the deposition of the silica-PNIPAM core–shell spheres. The core–shell colloidal dispersion is diluted 1:1 with ethanol as the spreading agent. The core–shell spheres are spread at the water-air interface on the Langmuir through until the surface is completely covered as evidenced by the onset of a rise in surface pressure. The interface is compressed by the barriers until a surface pressure of 32 mN/m is reached. The FTO coated glass slides are lifted at a speed of 10 mm/min. Last, the organic microgel shell is removed using oxygen plasma, resulting in a non-close packed hexagonal arrangement of silica spheres.

4.4. Additional samples

Anodic aluminum oxide membranes are grown from aluminum foil (99.999%) in a phosphoric acid (1%) electrolyte at 195 V at 0 °C as described elsewhere [39]. TiO_2 nanotubes (TiO_2NTs) are grown by anodizing sputtered Ti thin films on ITO/TiO_2 substrates as described elsewhere [21]. Native (100) silicon wafers (Silicon Materials Inc.) were cleaned by sonication in detergent (Hellmanex III, 2%), acetone, isopropanol, DI water and piranha acid (H_2SO_4/H_2O_2 3:1), for 10 min each. The surface was textured by etching with 2% NaOH, 20% isopropanol at 80 °C for 30 min as described elsewhere [40].

4.5. Characterization

Solar cell performance was measured under ambient conditions using a solar simulator (Newport, Xe lamp source) that was calibrated to AM1.5 at 100 mW cm^{-2} with a reference Si solar cell (Newport). A single-channel Gamry Reference 600 was used to record *JV*-curves with a scan speed of 50 mV/s from −0.3 to 1 V unless stated otherwise. An Oriel's QEPVSI-b system with a 300 W Xe light source, a monochromator and a lock-in amplifier was used to record EQE spectra. Electrochemical impedance was measured using a Gamry Interface 1000 potentiostat in the dark and under calibrated 1 sun (AM1.5) illumination using the same solar simulator with a frequency range from 1 MHz to 10 Hz. Capacitance–voltage (Mott-Schottky, MS) profiles were obtained in the dark at a frequency of 10 kHz. Recording *JV*-curves before and after impedance and MS ensure stability of the devices during the measurements. Stability data is shown in SI Fig. S43. All electrical characterization was performed without encapsulation in ambient atmosphere.

SEM micrographs were recorded with a Carl Zeiss field-emission SEM using an acceleration voltage of 2–5 kV. The SEM cross section was obtained by using a cross section polisher (Jeol IB-19530CP). Self-correlation was performed on the SEM micrographs using the software WSxM [41]. Cross sections for TEM were prepared by standard lift-out technique (ThermoFischer Helios Nanolab 660 dual beam focused ion beam (FIB)/SEM. HRTEM, STEM and EDX were performed at 300 kV using a Titan^3 Themis microscope (ThermoFischer) equipped with an ultrabright X-FEG electron source, spherical aberration correctors (both probeforming and imaging side). EDX spectra and maps were recorded on a SuperX detector array using a high probe current. Care was taken to avoid altering the sample structure by the intense electron beam. Optical microscopy images were recorded on a trinocular Motic BA310 with or without polarization filter.

X-ray photoelectron spectroscopy (XPS) spectra were measured with a PHI Quantera SXM X-ray photoelectron spectrometer from Physical Electronics Inc. equipped with an Al Kα source. The XPS spectra were fitted using the software CasaXPS (v2.3). All XPS spectra were corrected for charging effects by calibration with adventitious carbon (C 1s C–C, 284.8 eV). Raman measurements were conducted in ambient conditions in backscattering geometry using a Horiba T64000 spectrometer. For excitation, 532 nm wavelength was chosen (Laser Quantum); the laser

spot was focused to approximately 1 μm in diameter. The laser power was held between 0.1 mW and 0.4 mW for all measurements to prevent damage of the samples. Grazing incidence X-ray diffraction (GI-XRD) was performed at an incident angle of 0.7° using a (D8 DISCOVER X-ray diffractometer, Bruker) equipped with a Cu Kα source (20 kV) and a LynxEye XE T detector. UV/vis measurements were performed on planar films on glass substrates with a DH-2000-BAL light source from Ocean Optics with a HR 4000 detector equipped with a ISP-50-8-R integrating sphere. The thicknesses of the different layers deposited by ALD and sputtering were measured by spectroscopic ellipsometry (SENpro, Sentech).

CRediT authorship contribution statement

Pascal Büttner: Conceptualization, Data curation, Investigation, Writing – original draft, Writing – review & editing. **Florian Scheler:** Data curation, Investigation, Writing – review & editing. **Dirk Döhler:** Data curation, Investigation, Writing – review & editing. **Maïssa K.S. Barr:** Investigation, Writing – review & editing. **Michael Bosch:** Investigation, Writing – review & editing. **Marcel Rey:** Funding acquisition, Investigation, Writing – review & editing. **Tadahiro Yokosawa:** Data curation, Investigation, Writing – review & editing. **Sandra Hinz:** Data curation, Investigation, Writing – review & editing. **Janina Maultzsch:** Funding acquisition, Resources, Supervision, Writing – review & editing. **Erdmann Spiecker:** Resources, Supervision, Writing – review & editing. **Nicolas Vogel:** Funding acquisition, Resources, Supervision, Writing – review & editing. **Ignacio Mínguez-Bacho:** Conceptualization, Data curation, Funding acquisition, Supervision, Writing – original draft, Writing – review & editing. **Julien Bachmann:** Conceptualization, Data curation, Funding acquisition, Resources, Supervision, Writing – original draft, Writing – review & editing.

Declaration of competing interest

The authors declare that they have no known competing financial interests or personal relationships that could have appeared to influence the work reported in this paper.

Data availability

Data will be made available on request.

Acknowledgments

This work was supported by the European Research Council with a Consolidator Grant (‘Solacylin’, grant agreement 647281) and a Proof of Concept Grant (ALAMS - ‘Atomic-layer additive manufacturing of solar cells’, grant agreement 101069310) and by the European Commission with a Marie Skłodowska-Curie Grant (‘Hybricyl’, grant agreement 795716). M.R. acknowledges funding from the Swiss National Science Foundation Project-ID P2SKP2_194953. N.V. acknowledges support by the Deutsche Forschungsgemeinschaft (DFG) under grant number VO 1824/6-2. S.H. and J.M. acknowledge support by the Deutsche Forschungsgemeinschaft (DFG) under grant number LA 2901/5-1 and MA 4079/14-1.

Appendix A. Supplementary data

Supplementary material related to this article can be found online at https://doi.org/10.1016/j.nanoen.2022.107820. Supplementary data associated with this article can be found in the online version.

References

[1] S. Adachi (Ed.), Earth-Abundant Materials for Solar Cells: Cu2-ii-iv-vi4 Semiconductors, First Edition, John Wiley & Sons, Ldt. and The American Chemical Society, 2015.

[2] S. Giraldo, Z. Jehl, M. Placidi, V. Izquierdo-Roca, A. Pérez-Rodríguez, E. Saucedo, Progress and perspectives of thin film kesterite photovoltaic technology: A critical review, Adv. Mater. 31 (2019) 1806692, http://dx.doi.org/10.1002/adma.201806692.

[3] H. Lei, J. Chen, Z. Tan, G. Fang, Review of recent progress in antimony chalcogenide-based solar cells: Materials and devices, Solar RRL 3 (2019) 1900026, http://dx.doi.org/10.1002/solr.201900026.

[4] W. Yang, X. Zhang, S.D. Tilley, Emerging binary chalcogenide light absorbers: Material specific promises and challenges, Chem. Mater. 33 (2021) 3467–3489, http://dx.doi.org/10.1021/acs.chemmater.1c00741.

[5] W. Wang, M.T. Winkler, O. Gunawan, T. Gokmen, T.K. Todorov, Y. Zhu, D.B. Mitzi, Device characteristics of CZTSSe thin-film solar cells with 12.6% efficiency, Adv. Energy Mater. 4 (2014) 1301465, http://dx.doi.org/10.1002/aenm.201301465.

[6] Z.Q. Li, X.Y. Liang, G. Li, H.X. Liu, H.Y. Zhang, J.X. Guo, J.W. Chen, K. Shen, X.Y. San, W. Yu, R.E.I. Schropp, Y.H. Mai, 9.2%-Efficient core-shell structured antimony selenide nanorod array solar cells, Nature Commun. 10 (2019) 125, http://dx.doi.org/10.1038/s41467-018-07903-6.

[7] X. Wang, R. Tang, C. Jiang, W. Lian, H. Ju, G. Jiang, Z. Li, C. Zhu, T. Chen, Manipulating the electrical properties of Sb2(S,Se)3 film for high-efficiency solar cell, Adv. Energy Mater. 10 (2020) 2002341, http://dx.doi.org/10.1002/aenm.202002341.

[8] J. Han, S. Wang, J. Yang, S. Guo, Q. Cao, H. Tang, X. Pu, B. Gao, X. Li, Solution-processed sb2s3 planar thin film solar cells with a conversion efficiency of 6.9% at an open circuit voltage of 0.7 v achieved via surface passivation by a SbCl3 interface layer, ACS Appl. Mater. Interfaces 12 (2020) 4970–4979, http://dx.doi.org/10.1021/acsami.9b15148, PMID: 31698902.

[9] X. Wang, R. Tang, C. Jiang, W. Lian, H. Ju, G. Jiang, Z. Li, C. Zhu, T. Chen, Manipulating the electrical properties of Sb2(S,Se)3 film for high-efficiency solar cell, Adv. Energy Mater. 10 (2020) 2002341, http://dx.doi.org/10.1002/aenm.202002341.

[10] C. Chen, J. Tang, Open-circuit voltage loss of antimony chalcogenide solar cells: Status, origin, and possible solutions, ACS Energy Lett. 5 (2020) 2294–2304, http://dx.doi.org/10.1021/acsenergylett.0c00940.

[11] H. Deng, Y. Zeng, M. Ishaq, S. Yuan, H. Zhang, X. Yang, M. Hou, U. Farooq, J. Huang, K. Sun, R. Webster, H. Wu, Z. Chen, F. Yi, H. Song, X. Hao, J. Tang, Quasiepitaxy strategy for efficient full-inorganic Sb2S3 solar cells, Adv. Funct. Mater. 29 (2019) 1901720, http://dx.doi.org/10.1002/adfm.201901720.

[12] X. Jin, Y. Fang, T. Salim, M. Feng, S. Hadke, S.W. Leow, T.C. Sum, L.H. Wong, In situ growth of [hk1]-oriented Sb2S3 for solution-processed planar heterojunction solar cell with 6.4% efficiency, Adv. Funct. Mater. 30, 2002887, http://dx.doi.org/10.1002/adfm.202002887.

[13] J. Chen, J. Qi, R. Liu, X. Zhu, Z. Wan, Q. Zhao, S. Tao, C. Dong, G.Y. Ashebir, W. Chen, R. Peng, F. Zhang, S. Yang, X. Tian, M. Wang, Preferentially oriented large antimony trisulfide single-crystalline cuboids grown on polycrystalline titania film for solar cells, Commun. Chem. 2 (2019) 121, http://dx.doi.org/10.1038/s42004-019-0225-1.

[14] I. Massiot, A. Cattoni, S. Collin, Progress and prospects for ultrathin solar cells, Nature Energy 5 (2020) 959–972, http://dx.doi.org/10.1038/s41560-020-00714-4.

[15] H. Sai, T. Oku, Y. Sato, M. Tanabe, T. Matsui, K. Matsubara, Potential of very thin and high-efficiency silicon heterojunction solar cells, Prog. Photovolt., Res. Appl. 27 (2019) 1061–1070, http://dx.doi.org/10.1002/pip.3181.

[16] O.D. Miller, E. Yablonovitch, S.R. Kurtz, Strong internal and external luminescence as solar cells approach the Shockley–Queisser limit, IEEE J. Photovolt. 2 (2012) 303–311, http://dx.doi.org/10.1109/JPHOTOV.2012.2198434.

[17] K. Yoshikawa, H. Kawasaki, W. Yoshida, T. Irie, K. Konishi, K. Nakano, T. Uto, D. Adachi, M. Kanematsu, H. Uzu, K. Yamamoto, Silicon heterojunction solar cell with interdigitated back contacts for a photoconversion efficiency over 26%, Nature Energy 2 (2017) 17032, http://dx.doi.org/10.1038/nenergy.2017.32.

[18] J. Peng, D. Walter, Y. Ren, M. Tebyetekerwa, Y. Wu, T. Duong, Q. Lin, J. Li, T. Lu, M.A. Mahmud, O.L.C. Lem, S. Zhao, W. Liu, Y. Liu, H. Shen, L. Li, F. Kremer, H.T. Nguyen, D.-Y. Choi, K.J. Weber, K.R. Catchpole, T.P. White, Nanoscale localized contacts for high fill factors in polymer-passivated perovskite solar cells, Science 371 (2021) 390–395, http://dx.doi.org/10.1126/science.abb8687.

[19] H.-L. Chen, A. Cattoni, R. De Lépinau, A.W. Walker, O. Höhn, D. Lackner, G. Siefer, M. Faustini, N. Vandamme, J. Goffard, B. Behaghel, C. Dupuis, N. Bardou, F. Dimroth, S. Collin, A 19.9%-efficient ultrathin solar cell based on a 205nm-thick GaAs absorber and a silver nanostructured back mirror, Nature Energy 4 (2019) 761–767, http://dx.doi.org/10.1038/s41560-019-0434-y.

[20] C. Wu, K. Wang, M. Batmunkh, A.S.R. Bati, D. Yang, Y.Y. Jiang, Y.C. Hou, J.G. Shapter, S. Priya, Multifunctional nanostructured materials for next generation photovoltaics, Nano Energy 70 (2020) 104480, http://dx.doi.org/10.1016/j.nanoen.2020.104480.

[21] P. Büttner, D. Döhler, S. Korenko, S. Möhrlein, S. Bochmann, N. Vogel, I. Mínguez-Bacho, J. Bachmann, Solid state interdigitated Sb2S3 based TiO2 nanotube solar cells, RSC Adv. 10 (2020) 28225–28231, http://dx.doi.org/10.1039/D0RA04123H.

[22] Y. Itzhaik, O. Niitsoo, M. Page, G. Hodes, Sb2S3-sensitized nanoporous TiO2 solar cells, J. Phys. Chem. C 113 (2009) 4254–4256, http://dx.doi.org/10.1021/jp900302b.

[23] S.-J. Moon, Y. Itzhaik, J.-H. Yum, S.M. Zakeeruddin, G. Hodes, M. Grätzel, Sb2s3-based mesoscopic solar cell using an organic hole conductor, J. Phys. Chem. Lett. 1 (2010) 1524–1527, http://dx.doi.org/10.1021/jz100308q.

[24] D.U. Lee, S.W. Pak, S.G. Cho, E.K. Kim, S.I. Seok, Defect states in hybrid solar cells consisting of Sb2s3 quantum dots and TiO2 nanoparticles, Appl. Phys. Lett. 103 (2013) 023901, http://dx.doi.org/10.1063/1.4813272.

[25] P. Kaienburg, B. Klingebiel, T. Kirchartz, Spin-coated planar Sb2S3 hybrid solar cells approaching 5% efficiency, Beilstein J. Nanotechnol. 9 (2018) 2114–2124, http://dx.doi.org/10.3762/bjnano.9.200.

[26] J.S. Eensalu, A. Katerski, E. Karber, I.O. Acik, A. Mere, M. Krunks, Uniform Sb2S3 optical coatings by chemical spray method, Beilstein J. Nanotechnol. 10 (2019) 198–210, http://dx.doi.org/10.3762/bjnano.10.18.

[27] P. Büttner, F. Scheler, C. Pointer, D. Döhler, M.K.S. Barr, A. Koroleva, D. Pankin, R. Hatada, S. Flege, A. Manshina, E.R. Young, I. Mínguez-Bacho, J. Bachmann, Adjusting interfacial chemistry and electronic properties of photovoltaics based on a highly pure sb2s3 absorber by atomic layer deposition, ACS Appl. Energy Mater. 2 (2019) 8747–8756, http://dx.doi.org/10.1021/acsaem.9b01721.

[28] P. Büttner, F. Scheler, C. Pointer, D. Döhler, T. Yokosawa, E. Spiecker, P.P. Boix, E.R. Young, I. Mínguez-Bacho, J. Bachmann, ZnS ultrathin interfacial layers for optimizing carrier management in sb2s3-based photovoltaics, ACS Appl. Mater. Interfaces 13 (2021) 11861–11868, http://dx.doi.org/10.1021/acsami.0c21365.

[29] K.C. Gödel, B. Roose, A. Sadhanala, Y. Vaynzof, S.K. Pathak, U. Steiner, Partial oxidation of the absorber layer reduces charge carrier recombination in antimony sulfide solar cells, Phys. Chem. Chem. Phys. 19 (2017) 1425–1430, http://dx.doi.org/10.1039/C6CP07559B.

[30] N. Fleck, O.S. Hutter, L.J. Phillips, H. Shiel, T.D.C. Hobson, V.R. Dhanak, T.D. Veal, F. Jäckel, K. Durose, J.D. Major, How oxygen exposure improves the back contact and performance of antimony selenide solar cells, ACS Appl. Mater. Interfaces 12 (2020) 52595–52602, http://dx.doi.org/10.1021/acsami.0c14256, PMID: 33170631.

[31] D. Abou-Ras, T. Kirchartz, U. Rau (Eds.), Advanced Characterization Techniques for Thin Film Solar Cells, John Wiley & Sons, Ldt, 2016.

[32] P.P. Boix, A. Guerrero, L.F. Marchesi, G. Garcia-Belmonte, J. Bisquert, Current-voltage characteristics of bulk heterojunction organic solar cells: Connection between light and dark curves, Advanced Energy Materials 1 (2011) 1073–1078, http://dx.doi.org/10.1002/aenm.201100334.

[33] B. Lee, J. Hwang, J. Nam, S. Lee, J. Kim, S.-M. Koo, A. Baunemann, R. Fischer, M. Sung, Low-temperature atomic layer deposition of copper metal thin films: Self-limiting surface reaction of copper dimethylamino-2-propoxide with diethylzinc, Angew. Chemie Int. Ed. 48 (2009) 4536–4539, http://dx.doi.org/10.1002/anie.200900414.

[34] I. Massiot, A. Cattoni, S. Collin, Progress and prospects for ultrathin solar cells, Nature Energy 5 (2020) 959–972, http://dx.doi.org/10.1038/s41560-020-00714-4.

[35] J.S.J. Tang, R.S. Bader, E.S.A. Goerlitzer, J.F. Wendisch, G.R. Bourret, M. Rey, N. Vogel, Surface patterning with SiO2@PNiPAm core–shell particles, ACS Omega 3 (2018) 12089–12098, http://dx.doi.org/10.1021/acsomega.8b01985.

[36] Y.C. Choi, D.U. Lee, J.H. Noh, E.K. Kim, S.I. Seok, Highly improved Sb2S3 sensitized-inorganic–organic heterojunction solar cells and quantification of traps by deep-level transient spectroscopy, Adv. Funct. Mater. 24 (23) (2014) 3587–3592, http://dx.doi.org/10.1002/adfm.201304238, arXiv:https://onlinelibrary.wiley.com/doi/pdf/10.1002/adfm.201304238.

[37] P.P. Boix, Y.H. Lee, F. Fabregat-Santiago, S.H. Im, I. Mora-Sero, J. Bisquert, S.I. Seok, From flat to nanostructured photovoltaics: Balance between thickness of the absorber and charge screening in sensitized solar cells, ACS Nano 6 (2012) 873–880, http://dx.doi.org/10.1021/nn204382k, PMID: 22175224.

[38] V.M. Koch, M.K.S. Barr, P. Büttner, I. Mínguez-Bacho, D. Döhler, B. Winzer, E. Reinhardt, D. Segets, J. Bachmann, A solution-based ald route towards (ch3nh3)(pbi3) perovskite via lead sulfide films, J. Mater. Chem. A 7 (2019) 25112–25119, http://dx.doi.org/10.1039/C9TA09715E.

[39] K. Nielsch, J. Choi, K. Schwirn, R.B. Wehrspohn, U. Gösele, Self-ordering regimes of porous alumina: The 10 porosity rule, Nano Lett. 2 (2002) 677–680, http://dx.doi.org/10.1021/nl025537k.

[40] E. Muramoto, Y. Yamasaki, F. Wang, K. Hasegawa, K. Matsuda, S. Noda, Carbon nanotube–silicon heterojunction solar cells with surface-textured si and solution-processed carbon nanotube films, RSC Adv. 6 (2016) 93575–93581, http://dx.doi.org/10.1039/C6RA16132D.

[41] I. Horcas, R. Fernández, J.M. Gómez-Rodríguez, J. Colchero, J. Gómez-Herrero, A.M. Baro, WSXM: A software for scanning probe microscopy and a tool for nanotechnology, Rev. Sci. Instrum. 78 (2007) 013705, http://dx.doi.org/10.1063/1.2432410.